

A Study of the Noise Source Mechanisms in an Excited Mach 0.9 Jet - Complementary Experimental and Computational Analysis

Michael Crawley*, Rachelle L. Speth†, Datta V. Gaitonde‡, and Mo Samimy§

Mechanical and Aerospace Engineering, The Ohio State University, Columbus, OH

Coordinated experimental and numerical databases are analyzed concurrently to explore the dynamics of large-scale structure evolution and the resultant effect on the generated near-field pressure and far-field acoustic in a Mach 0.9 jet. The databases comprise an unheated jet which is being excited by plasma actuators in order to produce coherent structures with a well-defined phase. The dynamic interactions of the generated large-scale structures are investigated using phase-averaging and iso-contours of Q-criterion. The near-field is then decomposed into its constitutive hydrodynamic and acoustic components using a spatio-temporal wavelet transform. Two-point correlations between the full and decomposed near-field, and the near- and far-field acoustic are utilized to identify the dominant acoustic source regions in both jets. Our previous experimental work had shown that individual actuation event produce temporally and spatially localized pressure fluctuations in the irrotational near-field, which was termed the impulse response of the jet, and the response to periodic excitation could be reconstructed from a linear superposition of this impulse response. The preliminary analysis of the numerical results found that this same principle applied inside the jet shear layer, albeit with less accuracy; indicating that the structures interactions are largely linear in nature. Results also showed that the near- and far-acoustic fields are also governed by this quasi-linear mechanism (though that is not to say that the noise generation process itself is necessarily linear).

I. Introduction

Engine exhaust constitutes one of the major components of aircraft noise during takeoff and landing, and hence poses a significant health concern for community and military personnel. Mitigation of the aeroacoustic noise generated by free jets is therefore a necessity for both the commercial and military aviation industries. Current noise reduction technologies such as increased bypass ratios or geometric modifications to the nozzle (tabs, chevrons, and lobed mixers), though effective, have associated performance penalties in terms of added weight, drag, or loss of thrust - penalties that are incurred over the entire duration of the flight. A shift to active control technology is thus desirable in order to minimize the performance penalties while maximizing the noise reduction, however the proper application of control is not readily apparent. In the simulated two-dimensional shear layer of Wei & Freund [1] a generalized actuator was able to reduce the noise along a prescribed line in the acoustic field by up to 11 dB. The researchers observed that the excitation was not altering the broad characteristics of the shear layer (such as turbulent kinetic energy) or even the evolution of the most energetic structures in an appreciable manner. Rather, the control appeared to be affecting the acoustic field by regularizing the large-scale structures, thereby reducing the radiating efficiency of the noise sources. Clearly, fundamental understanding of the noise sources and radiating mechanisms is required for efficient and effective active noise mitigation strategies.

Perhaps the most well-known source model for jet mixing noise is the two-component model of Tam *et al.* [2], which recognized that the acoustic far-field spectra of jets can be represented as two distinct universal

*Graduate Research Assistant. Student Member, AIAA

†Graduate Research Assistant. Student Member, AIAA

‡John Glenn Chair Professor. Fellow, AIAA

§John B. Nordholt Professor. Fellow, AIAA

similarity spectra, irrespective of jet Mach number or temperature ratio. In this model, the incoherent fine-scale mixing layer turbulence, produces an incoherent, broadband acoustic field and is believed to be the dominant source of acoustic radiation at sideline angles. In contrast, aft angle radiation is dominated by the large-scale structures and exhibit a strong spectral peak. The spectra in between are combinations of the two, with a gradual shifting from one to the other. Theoretical analysis by Tam [3] demonstrated Mach wave radiation emitted through the supersonic convection of these large scale structures - the oft-mentioned "wavy-wall" analogy. This analysis was extended in Tam & Burton [4] to include amplification and decay of the structures, through which subsonically-convecting structures were found to emit noise (this structure evolution was also shown to broaden the directivity and frequency bands of the acoustic radiation). Experiments utilizing direct correlations between density and velocity fluctuations in the shear layers of high-speed jets and the acoustic far-field have supported this two-component source model [5, 6].

The recognition that the large-scale structures are the dominant noise sources in the turbulent jet is beyond doubt at this point. Yet, the exact dynamics that govern the evolution of the structures and ultimately the noise emission are still not fully understood. The intermittent nature of the structures and noise emission was first observed by Hileman *et al.* [7] in a supersonic jet. Simplified source models utilizing temporally and spatially modulated wavepackets were found to reproduce the superdirective character observed in the far-field spectra, as well as improve the match between the observed and predicted spectral amplitudes [8–10]. Hence, understanding the exact spatiotemporal evolution of the large-scale structures is important to predicting and ultimately controlling their radiation production.

The ability to perturb the jet shear layer, in effect controlling the temporal and azimuthal frequency content of the large-scale structures, may thus serve as a useful tool for noise source analysis. Localized arc-filament plasma actuators (LAFPAs) have been developed at the Gas Dynamics and Turbulence Laboratory for use in high-speed flow control applications. Unlike traditional acoustic drivers, LAFPAs have been shown to produce high amplitude and high frequency excitation signals suitable for controlling the shear layer development of high Mach number and high Reynolds number jets [11–14]. These actuators have successfully been used for both mixing enhancement and noise mitigation in laboratory scale subsonic and supersonic jets; a review of the development of LAFPAs and their use in high-speed jet flow control can be found in Samimy *et al.* [15]. Additional to their noise mitigation and mixing enhancement potential, LAFPAs have been used as diagnostic tools for understanding the large-scale structure dynamics and noise production mechanisms in high-speed jets. Kearney-Fischer *et al.* [16] utilized a phase-locked schlieren imaging system to LAFPA excitation in a heated, subsonic jet in order to study the Mach-wave-like compression waves generated by the large-scale structures. By varying the frequency and Fourier mode of the forcing, the effect of structure characteristics on the radiated noise was evaluated. Sinha *et al.* [17] investigated the dynamics of large-scale structure interactions in a Mach 0.9 jet by phase-averaging the near-field pressure signals from a linear microphone array. It was found that for low to moderate forcing Strouhal numbers ($St_{DF} < 0.5$), each excitation pulse produced a single structure, the near-field signature of which was a compact waveform. The waveform shape and amplitude at moderate forcing Strouhal numbers were found to be well-predicted by a linear superposition of the impulse response of the jet to excitation ($St_{DF} < 0.1$). This analysis was extended to the acoustic near- and far-field in Crawley *et al.* [18], in which it was found that the acoustic field could also be represented as a linear superposition of the impulse response of the jet, and that the dominant noise source region shifted upstream with increasing Strouhal number.

Concurrent to this work, the High Fidelity Computational Multi-Physics Laboratory (HFCMPL) has developed a large eddy simulation solver (FDL3DI) to simulate the effect of the LAFPAs on the jet shear layer. Validation of the numerical method and initial comparisons of the simulated and experimental results were performed in Gaitonde & Samimy [19] and Speth and Gaitonde [20]. In the recent studies of Speth and Gaitonde [20,21], the LAFPAs were pulsed at low frequencies to analyze the impulse response and at relatively higher frequencies ($St_{DF} > 0.15$) to study the manner in which the structures begin to interact. The large coherent structures of the jet were linked to the near field through analysis of phase-averaged waveforms and correlations. The correlations described the development and interaction of subsequent structures in time and space. The higher frequency of excitation tested ($St_{DF} = 0.25$) created a narrower correlated region than the low frequency cases due to the organized development and decay of the large scale structures. This region extended from the end of the potential core to the 30 degree near field. Compressibility effects were also investigated in Speth & Gaitonde [20] and found that the supersonic case has higher correlations throughout the near field than the subsonic cases.

The current work represents the first stage in assimilating analyses from the experimentally- and numerically-

acquired results to use the strengths of both techniques (i.e. long time traces for experiments and spatial resolution for simulations) to obtain a deeper knowledge of noise production of a jet. First, we begin by describing the experimental and computational setup in Sections II and III. Then the evolution of the large scale coherent structures is analyzed in Section IV.A, while the acoustic component of the near field is analyzed in Section IV.B.

II. Experimental Setup

Experimentation was conducted in the free jet facility (a schematic of which can be found in Fig. 1) at the Gas Dynamics and Turbulence Laboratory (GDTL) within the Ohio State University's Aerospace Research Center. The dimensions of the chamber are 5.14 m wide by 4.48 m long and 2.53 m high (wedge-tip to wedge-tip). The design of the chamber produces an anechoic cutoff frequency of 160 Hz, below the frequencies of interest for this study. Additional details of the facility design and validation can be found in Hahn [22]. Compressed, dried, and filtered air is supplied by two cylindrical storage tanks with a total capacity of 43 m³ and maximum pressure of 16 MPa; the tanks are charged by three, five-stage reciprocating compressors. The air enters the facility horizontally, passes through a stagnation chamber and turbulence screens, and exhausts through a converging nozzle. Opposite the nozzle, a collector accumulates the jet and entrained air and exhausts to the outdoors.

A converging, axisymmetric nozzle with exit diameter of 25.4 mm was used in the current study. The internal contour of the nozzle was designed using a fifth order polynomial. The nozzle utilized a thick-lipped design in order to simplify the mounts for the LAFPA extension, which housed the eight actuators used in this study. For the experiments reported in this paper, the jet was operated at a Mach number, M_j , of 0.90, and with a total temperature ratio of unity. The Reynolds number based on the jet exit diameter was 6.2×10^5 ; previous investigations using hot-wire anemometry have indicated that the initial shear layer is turbulent for this operating condition with momentum thickness 0.09 mm and boundary layer thickness 1 mm [23].

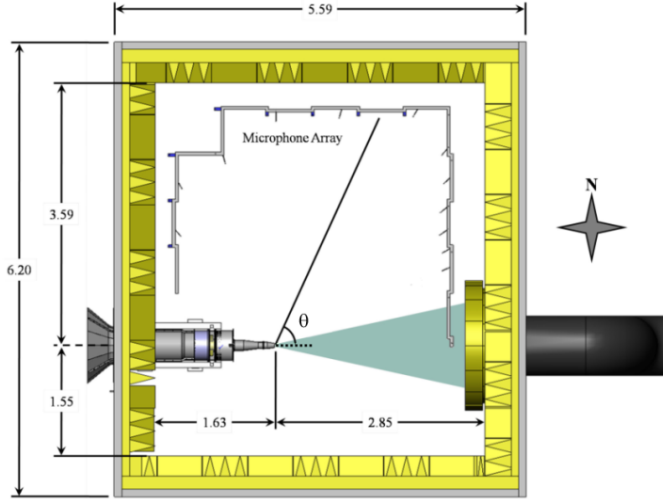


Figure 1: Plan view of GDTL free jet facility; dimensions in meters.

Excitation was applied to jet shear layer via eight LAFPAs which were uniformly spaced around the nozzle perimeter 1 mm upstream of the nozzle exit. Each LAFPA consists of a pair of tungsten pin electrodes with tip spacing (center-to-center) of 4 mm. The electrodes are housed in a boron nitride extension attached to the end of the nozzle. A more detailed description of LAFPA characteristics can be found in Utkin et al. [24]. The LAFPAs are energized by a multi-channel, high-voltage plasma power generator capable of simultaneously powering up to eight LAFPAs, which was designed and built in-house at the GDTL. In the second-generation power supply, each individual circuit consists of a switchable capacitor in line with a high voltage transformer; the arcing electrodes are connected to the secondary side of the coil. The switches are

controlled by a 16-channel digital I/O card and National Instruments' Labview software, operated by a dedicated computer. The plasma generator provides independent control of the frequency, duty cycle/pulse width, and phase of each individual actuator (though at a constant amplitude of 5 kV). The pulse width was held constant at $7 \mu\text{s}$, which was found to be the minimum pulse width at which the actuators consistently arced for all frequencies explored in this study [25]. In order to improve our understanding of the linear and nonlinear dynamics of the large-scale structure interactions, the excitation Strouhal numbers ranges from 0.02 to 0.50; an azimuthal mode of $m = 0$ was used in all cases.

Near-field and far-field pressure measurements were acquired simultaneously, using Brüel & Kjær 1/4 inch 4939 microphones. The signal from each microphone is band-pass filtered from 20 Hz to 100 kHz using a Brüel & Kjær Nexus 2690 conditioning amplifier, and recorded using National Instruments PXI-6133 A/D boards and LabView software. The microphones are calibrated using a Brüel & Kjær 114 dB, 1 kHz sine wave generator. The frequency response of the microphones is flat up to roughly 80 kHz, with the protective grid covers removed. Voltage signals are collected at 200 kHz with 81920 data points per block; sub-blocks of 8192 data points were used when calculating short-time power spectral densities, resulting in a frequency resolution of 24.4 Hz. Ten blocks were recorded for each case, resulting in four seconds of data. Analysis of the far-field acoustic spectra found this length to be sufficient for statistical convergence of the turbulence statistics.

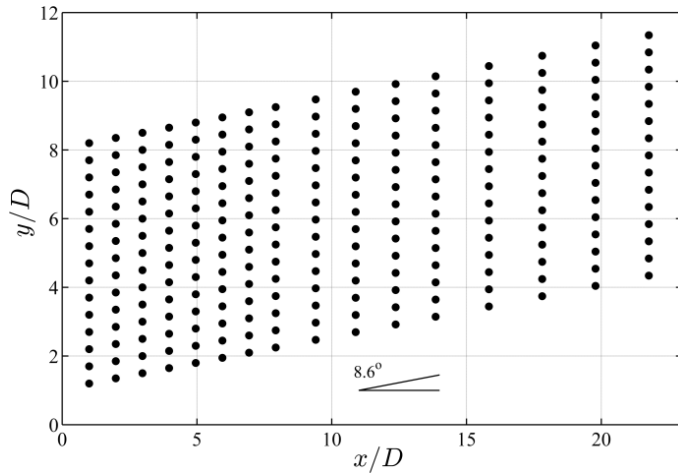


Figure 2: Near-field microphone array grid.

Far-field acoustic pressure is acquired at three polar angles: 30° , 60° and 90° , as measured from the downstream jet axis. The radial distance of the microphones ranges from $101D$ at 30° to $145D$ at 60° . The near-field pressure was acquired using a linear array of sixteen microphones located along the meridional plane of the jet; the spacing varied along the array from $1D$ to $2D$ (Fig. 2). The linear array is mounted to a traverse system at an angle of 8.6° to the jet axis in order to match the spreading angle of the jet shear layer for this Mach number [23]. The traverse is controlled using LabView and enables the acquisition of pressure measurements at various radial positions with respect to the jet axis. Initially, the most upstream microphone is positioned at $x/D = 1$ and $r/D = 1.20$, to ensure that the microphone tips are outside the mixing layer and do not affect the flow field. For subsequent cases, the microphone array is incremented radially outward by $0.5D$ for a total travel distance of $7D$. Signals from the near-field array are preprocessed in order to remove actuator-self noise while retaining the true hydrodynamic and acoustic response of the jet. This has been accomplished via a filter operating in the continuous wavelet domain. Further details may be found in Crawley et al. [18].

III. Computational Model

The simulations employ the same approach as previously used to simulate a Mach 1.3 jet without and with control [19, 26]. The full compressible Navier-Stokes equations are solved in curvilinear coordinates (ξ, η, ζ) using the strong conservative form [27, 28]. The transformed non-dimensional equations in vector

notation are given as:

$$\frac{\partial}{\partial \tau} \left(\frac{\vec{U}}{J} \right) + \frac{\partial \hat{F}}{\partial \xi} + \frac{\partial \hat{G}}{\partial \eta} + \frac{\partial \hat{H}}{\partial \zeta} = \frac{1}{Re} \left[\frac{\partial \hat{F}_v}{\partial \xi} + \frac{\partial \hat{G}_v}{\partial \eta} + \frac{\partial \hat{H}_v}{\partial \zeta} \right] \quad (1)$$

where $\vec{U} = \{\rho, \rho u, \rho v, \rho w, \rho E\}$ denotes the solution vector and $J = \partial(\xi, \eta, \zeta, \tau) / \partial(x, y, z, t)$ is the transformation Jacobian. Details of the various terms in Eqn. 1 may be found in Speth and Gaitonde [29]. For the inviscid terms, a third-order upwind biased approach is adopted, together with the Roe scheme [30] for flux evaluation. The limiter required to enforce monotonicity is a crucial component of the method. The van Leer harmonic limiter [31] has proven to be very successful at reproducing the main features of the unsteadiness in the jet. The viscous terms are discretized with second-order centered differences and time integration is performed by a second-order diagonalized [32] approximately factored method [33]. A sub-iteration strategy is used to minimize errors due to factorization, linearization and explicit boundary condition implementation.

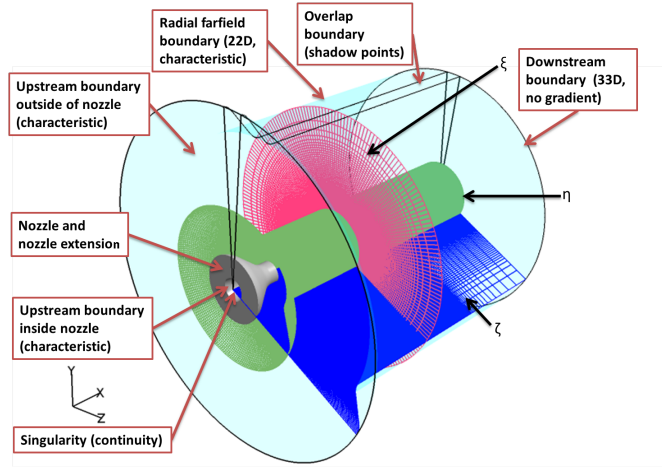


Figure 3: Computational domain

A 65 million point mesh (Fig. 3) is used to simulate the Mach 0.9 jet measured in the experiment (Fig. 1). The grid has dimensions of 685 points on the ξ (streamwise) direction, 455 points in the η (radial) direction, and 209 points in the ζ (azimuthal) direction. In the radial direction, the mesh is refined in the nozzle region and gradually stretched in the far field. At the exit of the nozzle, the grid maintains a constant axial spacing until after the potential core length; then stretches in the streamwise direction. To preserve continuity, the grid has a five point overlap in the ζ direction. Characteristic boundary conditions [34] are applied to the upstream (outside the nozzle) and radial boundaries. Non-reflecting conditions are applied to the downstream and far-field boundaries. Stagnation conditions are specified at the first ξ plane of the nozzle ($\rho_{inlet} = 2.04 \text{ kg/m}^3$, $U_{inlet} = 22 \text{ m/s}$, $P_{inlet} = 171,427 \text{ Pa}$) to achieve perfectly expanded nozzle exit conditions corresponding to $\rho_{jet} = 1.404 \text{ kg/m}^3$, $U_{jet} = 285.99 \text{ m/s}$, $T_{jet} = 251.31 \text{ K}$ which match the experiments. Based on the nozzle diameter therefore, the Reynolds number is $Re = 635,308$. The nozzle geometry resembles that of the experiments including the nozzle ring on which the actuators are mounted. The velocity profile at the entrance to the nozzle is that of a uniform flow (zero at the wall and U_{inlet} everywhere else). Perturbations were not introduced into the inflow due to the unknown perturbations in the experiment. Therefore, the simulations have a laminar boundary layer at the nozzle exit while the experiments have a very thin turbulent boundary layer (the momentum thickness has been estimated to be 0.09mm). Previous studies have shown that despite this difference, the main features of the experimental observations are successfully reproduced by the computations [19, 26]. Other studies have shown that a smaller 32 million point simulation is adequate to reproduce the features of the experiment [21].

The LAFPAs are modeled after the experiments using a surface heating technique to excite jet shear layer instabilities and azimuthal modes within the jet. Eight actuators are placed around the periphery of the jet on the nozzle collar at the locations and dimensions of the experiments as explained previously. As shown in Fig. 4b, each actuator consists of a heated region of the nozzle wall which extends the azimuthal

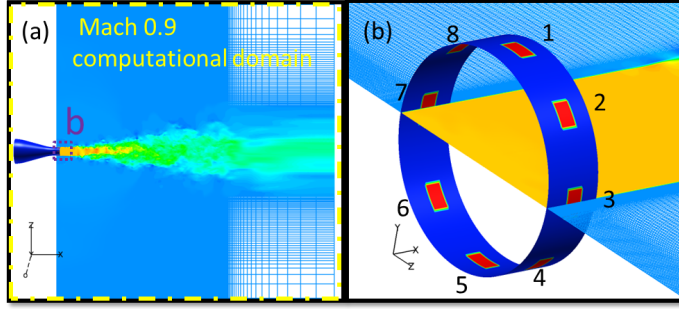


Figure 4: The computational domain including the nozzle (a), and the numerical actuator model (b)

length corresponding to the separation distance between electrodes (3mm) and has an axial extent equal to the length of the groove (1mm). The temperature of the nozzle wall was assumed to be $1.12T_{\infty}$. When the actuator is on the temperature of the actuator region increases to $5T_{\infty}$. Little difference was seen in the previous work (Speth and Gaitonde [35]) for the temperature range measured in experiments (Utkin *et al.* [12]) for a Mach number of 1.3. The semi-empirical model is necessary to avoid first-principles simulation of the poorly understood plasma heating process, as well as to restrict the required computational resources to feasible levels (see Ref. [36]).

Unlike acoustic drivers, the LAFPAs are on-off devices and thus can be represented by rectangular pulses with a duty cycle, which allows for a wide range of operation choices. Duty cycle is the percentage of actuator on time in an excitation cycle. Therefore, a duty cycle of 100% results in the actuator being on all the time. The experimental duty cycle varies with frequency, since the arc strike lasts a fixed time. Since the actuator model is empirical, the computational duty cycle was chosen to obtain similar control authority as in the experiment. This necessitates a higher duty cycle (10%) than the one used in the experiments (2.0% for $St_{DF} = 0.25$). As noted earlier, despite the simplicity of the model, its success has been documented in Gaitonde and Samimy [19], where, in addition to coherent structures, mean and fluctuating quantities have been compared. Furthermore, the mean flow structure with control was shown to match the theoretical predictions of Cohen and Wygnanski [37].

Like the experiments, the axisymmetric ($m = 0$) mode was employed to study a range of Strouhal numbers. The Strouhal numbers studied in the simulations include: 0.05, 0.15, and 0.25. Data was acquired every timestep at the point probes depicted in Fig. 2 as well as on several ξ , η , and ζ computational planes. Phase-averaged data were also computed for each of the simulations.

IV. Results

IV.A. Evolution of the Large-Scale Structures

The work of Sinha *et al.* [17] was the first to identify and characterize the temporal signature of large-scale structures in the irrotational near-field of a turbulent, Mach 0.9 jet excited by plasma actuators. They found that each excitation pulse produced a well-defined compact waveform which could easily be recovered from the natural turbulent fluctuations by phase-averaging, a process similar to the triple decomposition of Hussain & Reynolds [38]. When the jet is excited at very low frequencies ($St_{DF} < 0.1$), the characteristic period of the waveform is much shorter than the excitation period. As a result, the structures seeded by the excitation do not interact with one another as they evolve downstream; this behavior was coined the "impulse" response of the jet by the researchers. As the excitation frequency is increased the structures begin interacting, resulting in a periodic waveform with a corresponding reduction of the characteristic structure time and, ultimately, amplitude. Interestingly, it was observed that for moderate excitation frequencies ($St_{DF} \leq 0.5$) this periodic waveform could be well-predicted by a simple linear superposition of impulse waveforms.

The impulse and periodic phase-averaged waveforms can be observed in Fig. 5a, where the experimental data have been plotted along the first microphone array position at $x/D = 3$, over a large range of excitation frequencies. Here, and throughout the rest of the paper, the pressure has been normalized by the

jet dynamic head, $p^* = p/\rho_j U_j^2$. Additionally, a linear superposition of the impulse response observed for $St_{DF} = 0.02$ has been plotted against the periodic response observed at $St_{DF} = 0.5$ in Fig. 5b. While the waveform shape, temporal extent, and amplitude are all significantly altered from the impulse response, the dynamics which govern the periodic response of the jet in the irrotational near-field behave predominantly in a quasi-linear manner.

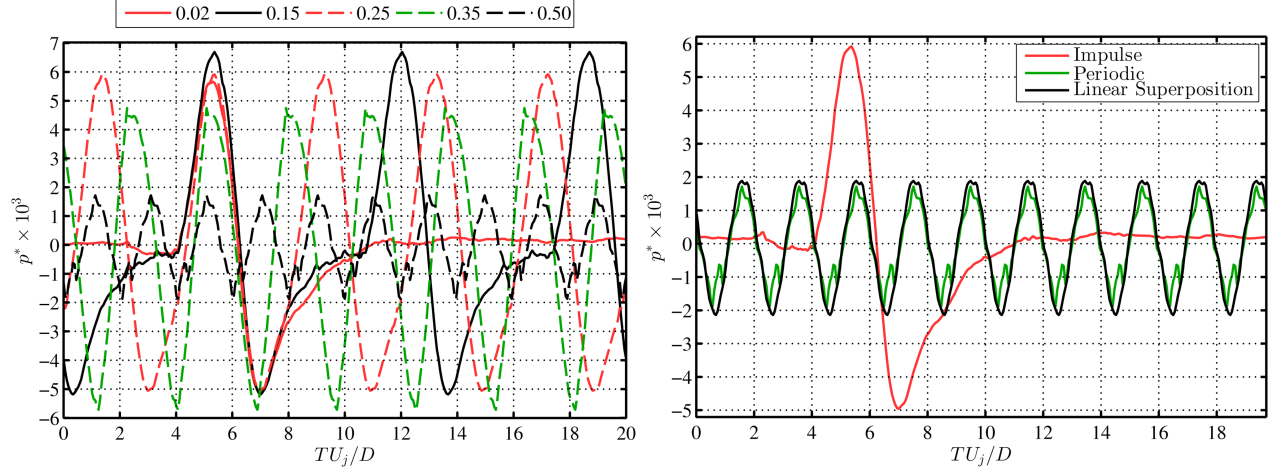


Figure 5: Phase-averaged waveforms at $x/D = 3$, $r/D = 1.5$ in the experimental results (a) and an example of superposition for excitation at $St_{DF} = 0.5$ (b).

While the behavior observed in Figs. 5 sheds new light on the structure evolution and interactions which are ultimately responsible for the acoustic emission, the view provided by the irrotational near-field pressure represents a spatially filtered view of the large-scale structure dynamics due to the strong spatial decay of the evanescent wave produced by the structures [39]. Thus, it is desirable to explore this process directly inside the shear layer in order to get an unadulterated view of the dynamic process by which the large-scale structures transfer energy to the acoustic field. The LES results are indispensable in this regard, as they can provide temporally-resolved, high-fidelity results inside the jet mixing layer, far beyond what is obtainable with current experimental technology.

As a first step, the phase-averaged waveforms have been plotted along the lipline in Fig. 6a for the same axial locations as in Fig. 5a. Also, the linear superposition model was evaluated along the jet lipline in the simulated results; this can be seen in Fig. 6b. Note that there are several differences between the experimental and numerical results. Foremost among these is the state of the boundary layer as it exits the nozzle. In the experimental jet, the boundary layer has been determined to be fully turbulent [23]. However, the detailed experimental exit velocity profile properties are not available and therefore the numerical simulations do not include a turbulent exit boundary layer within the nozzle. It was shown in Ref. 20 that this difference requires a fixed shift in the longitudinal coordinate for the computational results to match those of the experiments. The sensitivity of the actuated jet response to the exit state and actuator model are currently being studied. Note also that Fig. 6b has superpositioning related to a $St_{DF} = 0.25$ for the periodic response while the experiments plotted in Fig. 5b use a $St_{DF} = 0.5$. Lastly, due to computational requirements, the simulation time lapse is far shorter than the length of time recorded in the experimental results, resulting in a more jagged phase-averaged profile.

As a result, it is not expected that the individual waveform shapes or amplitudes will match exactly between the two data sets, and indeed they do not: the impulse response observed in Fig. 5 is quite unlike the impulse response observed in Fig. 6. Nonetheless, the linear superposition model still provides good overall match to the periodic response at $St_{DF} = 0.25$, which was the highest frequency explored in the simulations. The waveform shape and amplitude are well predicted by the linear superposition, with one noticeable caveat: the periodic response exhibits dual compression waves. While the linear superposition does produce a secondary compression peak, it is far less prominent. Given the much greater amplitude of the pressure fluctuations along the jet lipline as compared to the irrotational near-field, it is perhaps unsurprising that nonlinear effects play a greater role. However, the interaction between the structures still appears to be governed predominantly by quasi-linear dynamics.

A broad view of the interactions between the coherent structures generated by the excitation can be

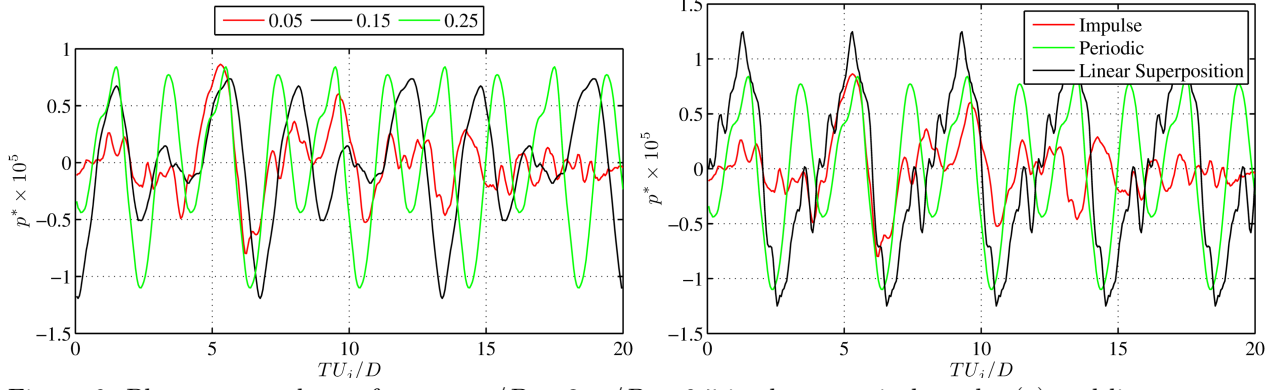


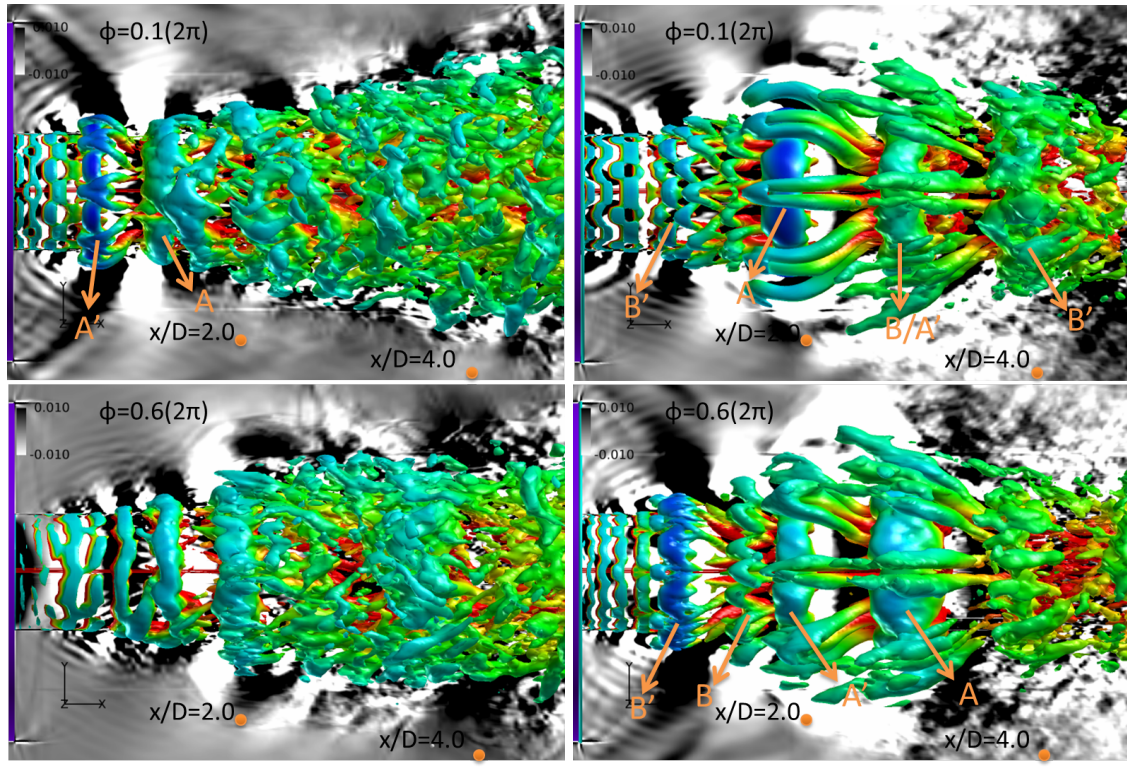
Figure 6: Phase-averaged waveforms at $x/D = 3$, $r/D = 0.5$ in the numerical results (a) and linear superposition of the impulse response as compared against the periodic response at $St_{DF} = 0.25$ (b).

easily identified by visualizing isolevels of Q-criterion ($Q = 0.35$), colored by axial velocity and overlaid on the dilatation field in gray scale. This has been depicted in Fig. 7 for $St_{DF} = 0.05$ and 0.25 , using the phase-averaged results. Each figure depicts two phases of the excitation period ($\phi = 0.2\pi$ and 1.2π). At each phase, the locations $x/D = 2$ and 4 of the first array are labeled. For the $St_{DF} = 0.05$ cases (Fig. 7a), the A' and A structures are labeled at phase 0.2π . At phase 1.2π , the structure observed during the first phase has already either broken up or developed significant jitter in their phase, resulting in no observable actuator induced structures at this phase for this Strouhal number.

Figure 7b depicts the isolevels of the high frequency ($St_{DF} = 0.25$) case. Rollers develop due to the excitation that grow and interact with other actuator induced structures as they propagate downstream. Initially, the structures that are produced at phase $\phi = 1.2\pi$ of Fig. 7b are similar to those associated with the impulse response (Fig. 7a). However, as each structure grows and propagates downstream, it interacts with the structure generated during the prior actuator on event. Thus structures B and B' are equivalent to A and A' respectively, but belong to the previous/subsequent actuator pulse. Since the reaction to the actuation is cyclic, the structures seen at the end of the potential core at one phase ($\phi = 0.2\pi$) begin to develop at similar phases in the next cycle. Structure B/A' in phase $\phi = 0.2\pi$ occurs when structure B collides into structure A'. This compression occurs due to the relatively high convective velocity of B (which is closer to the nozzle exit where the speed is higher) compared to A' which has encountered more entrainment. This interaction is quasi-linear, creating a sine-like response in the near-field pressure through linear superposition of the two actuator structures (B and A').

The structures affect the near-field as seen by the strong dilatation waves surrounding each large scale structure. The dilatation values of Fig. 7 may be connected to the pressure profiles of Fig. 6. The white dilatation waves (lower dilatation value) correspond to an increase in pressure while the black dilatation waves (higher dilatation value) correspond to a decrease in pressure. These pressure fluctuations can be readily seen in the phase-averaged pressure probes along the first array. At a phase of $\phi = 0.2\pi = 36^\circ$ in Fig. 7b, the $x/D = 4$ point probe is entering a white dilatation region (increase of pressure) while the $x/D = 2$ probe is entering a black dilatation wave corresponding to a decrease in pressure.

While these structures cannot be compared directly to the turbulence of the natural jet owing to the lack of a phase-reference, the evolution of the fluctuation intensity (mean-squared pressure, P_{ms}) can serve as a simple, if coarse, metric for comparison between the natural and excited structures. The results for the experimental and numerical results are shown in Fig. 8 along the first pressure probe array for the different excitation Strouhal cases and the natural jet (indicated in the figure as 0.00). Similar trends are found for the simulated results, though quantitative differences exist for each Strouhal number. The mean square pressure increases with increasing excitation Strouhal number until the column mode Strouhal number is reached ($St_{DF} \approx 0.3$) at which point the mean square pressure starts to decrease with increasing excitation Strouhal number. Although the computations do not consider Strouhal numbers higher than the most amplified column mode value, we note that in an earlier numerical study a similar reduction in control authority was observed at higher excitation frequencies [26] and the near field pressure fluctuations were also diminished [40]. For both experiments and simulations, increasing the excitation Strouhal number also



(a) $St_{DF} = 0.05$

(b) $St_{DF} = 0.25$

Figure 7: Simulations of the phase averaged iso-levels of Q-criterion colored by axial velocity with gray scale of dilatation at excitation $St_{DF} = 0.05$ (a) and 0.25 (b)

yields an upstream shift in the saturation location. In the case of the unforced jet, the fluctuations peak at $x/D = 5$, just upstream of the end of the potential core, and slowly decays beyond that point. Excitation at the lowest frequencies, where the structures do not undergo significant quasi-linear interactions, results in an amplification of the fluctuation energy over nearly the entire domain, though it is most significant near the saturation point. In this case, the saturation point has shifted upstream, to $x/D = 4$, and displays a slightly sharper peak. These results are consistent with those of other researchers, who have shown that perturbations of higher frequencies saturate earlier upstream than lower frequencies [41, 42].

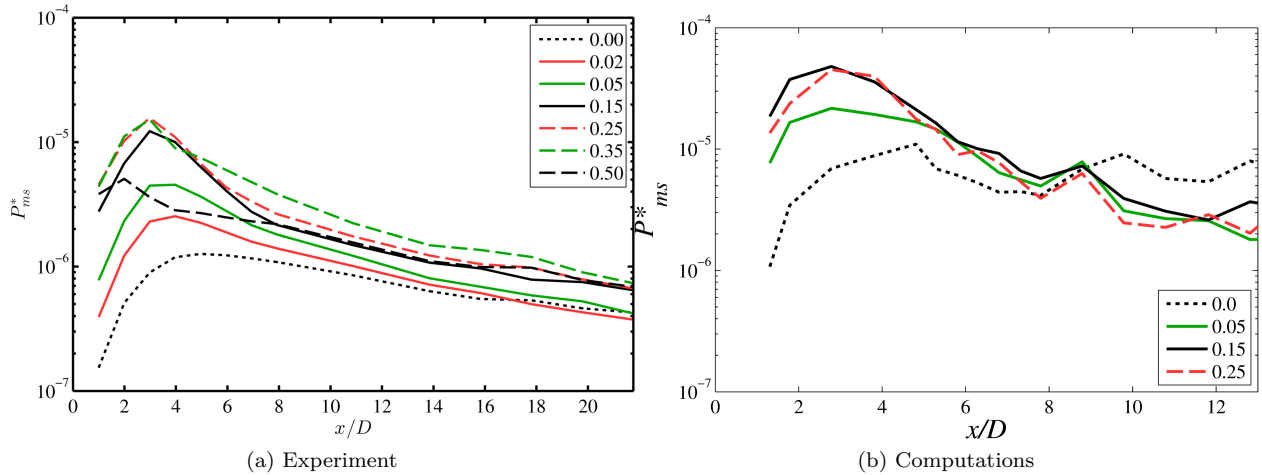


Figure 8: Mean-square pressure along the first array (first probe located at $r/D = 1.2$) for experimental (a) and computational results for various excitation Strouhal numbers. The baseline case is shown with 0.00.

IV.B. Identification of the Acoustic Response

In Crawley *et al.* [18] the work of Sinha *et al.* [17] was extended to the acoustic far-field, where it was found that the excitation again produced a coherent response in the acoustic field, and a linear superposition of the impulse response well-predicted the periodic response, at least at aft angles. This behavior is demonstrated in Fig. 9 for a polar angle of 30° in the experimental jet. As with the irrotational near field (which is dominated by hydrodynamic fluctuations), the acoustic far field exhibits a compact waveform for the lowest excitation Strouhal numbers. The behavior of the far-field response did diverge from the near-field in one distinct metric: in the case of the far-field response the linear superposition model was able to predict the periodic response only up to $St_{DF} = 0.25$. The reason behind this is currently not well understood - nonlinear dynamics may become significant to the acoustic emission process beyond this frequency, or the structures at this frequency are no longer radiating efficiently (the far-field spectra peaks around $St_{DF} = 0.15$), or there may be greater jitter in the acoustic response, and as a result the acoustic response is lost in the phase-averaging process.

In order to identify the origin of the far-field acoustic emissions (both spatially and temporally), a decomposition of the near-field is desired, as the strong hydrodynamic pressure fluctuations associated directly with the passage of coherent structures largely mask the resultant weak acoustic radiation. As has been shown by Arndt *et al.* [39], the irrotational near field of the jet comprises both the hydrodynamic footprint of the large-scale structures in the mixing layer as well as acoustic radiation. The analysis of Coiffet *et al.* [43] showed that the total near field can be thought of as a linear superposition of the hydrodynamic and acoustic fields. Therefore, a suitably designed linear filter can, in principle, extract the constitutive fields from the experimentally measured near field.

This was first done experimentally by Tinney & Jordan [44], using a linear array of microphones and a wavenumber-frequency filter in the Fourier domain to separate the irrotational near-field into subsonically- and supersonically-convection waves. The author's justification for this algorithm was that in an unheated subsonic jet, the hydrodynamic pressure fluctuations will be aligned with the jet axis, and travelling subsonically. Acoustic pressure fluctuations will impinge on the linear microphone array at oblique angles and therefore will appear as having either sonic or supersonic phase velocity based on the source location. In the current work a similar method is used, though the two-dimensional Fourier transform has been replaced

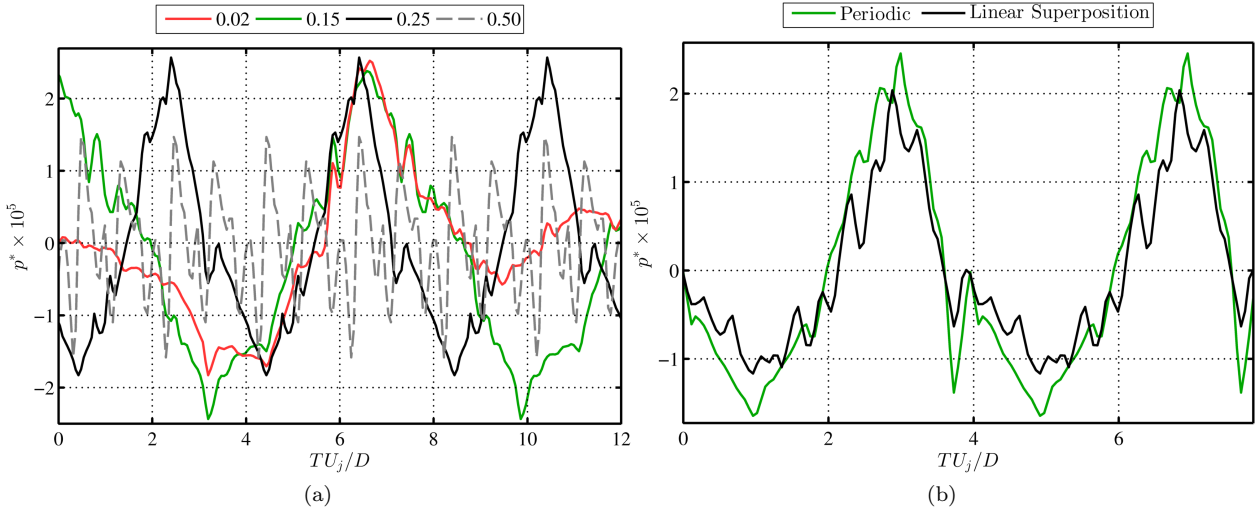


Figure 9: Far-field response to excitation at 30° in the experimental jet, phase-averaged waveforms (a) and linear superposition of the impulse response ($St_{DF} = 0.02$) against the periodic response at $St_{DF} = 0.25$.

with a spatio-temporal wavelet transform [45]. Sample results for this decomposition can be found in Fig. 10 for the experimental results. Here, the full near-field pressure and the acoustic component of the irrotational near-field have been plotted against the far-field acoustic, in the spectral domain in the case of the natural jet and with phase-averaged waveforms in the jet excited at $St_{DF} = 0.02$. The near-field signals were scaled in amplitude based on the propagative distance from the near-field microphone ($x/D = 8, y/D = 2.2$) in order to account for spherical propagation of the waves. This requires an assumption on the acoustic source region, which is not known with certainty. For the current work, the noise source location was assumed to be centered around $x_s/D = 4, y_s/D = 0$; the reasoning for this assumption will become more clear in short order.

The decomposition method accurately reproduces the high-frequency content acoustic spectrum, which is unsurprising given that the near-field spectra are dominated by acoustic fluctuations over this range of frequencies (though this does reinforce the accuracy of the amplitude-scaling explained previously). In contrast, the acoustic spectral peak is masked in the near-field by the far more dominant hydrodynamic field. Though imperfect, the decomposition does a good job capturing the peak amplitude, frequency, and low-frequency decay of the true acoustic field. The impulsive excitation provides an additional opportunity to validate the decomposition, this time in the temporal domain. Phase-averaged waveforms for the far field, full near field and acoustic near field have also been analyzed in Fig. 10b for the jet excited at $St_{DF} = 0.02$. Again, the filtered acoustic signal does differ somewhat from the far-field acoustic signal. However, the overall agreement is remarkable, particularly considering the waveform amplitude and shape differs significantly from the full near-field signal. Clearly, the decomposition algorithm is preserving not only the spectral content but statistically non-stationary events in the acoustic near field. Additional details of the decomposition algorithm and validation in the experimental results can be found in Crawley & Samimy [45].

A robust linkage directly between the hydrodynamic fluctuations and the noise emission is not a straightforward affair. However, initial associations can be made with two-point correlations between the near field and the far field. This was performed in the experimental jet for the closest array position to the far field at 30° and the correlations were then examined in the spatio-temporal domain. Distinct regions of positive and negative correlation spanning several jet diameters and flow time scales are observed with drastically differing slopes, indicating differing propagation mechanisms. Similar to the work of Bogey & Bailly [46], the physical phenomena to which these correlation regions correspond can be identified by comparing their slopes against the convective velocity of the large scale structures (indicated by τ_{con}) and the ambient speed of sound (indicated by τ_{ac} for on-axis propagation between the near-field and the far field microphones and by τ_s for off-axis propagation). For simplicity, diffraction and convection effects have been neglected in this analysis. The convection velocity was assumed to be $U_c = 0.69U_j$; this value was determined from two-point correlations between adjacent microphones located in the most upstream region of the jet ($x/D \leq 5$). The

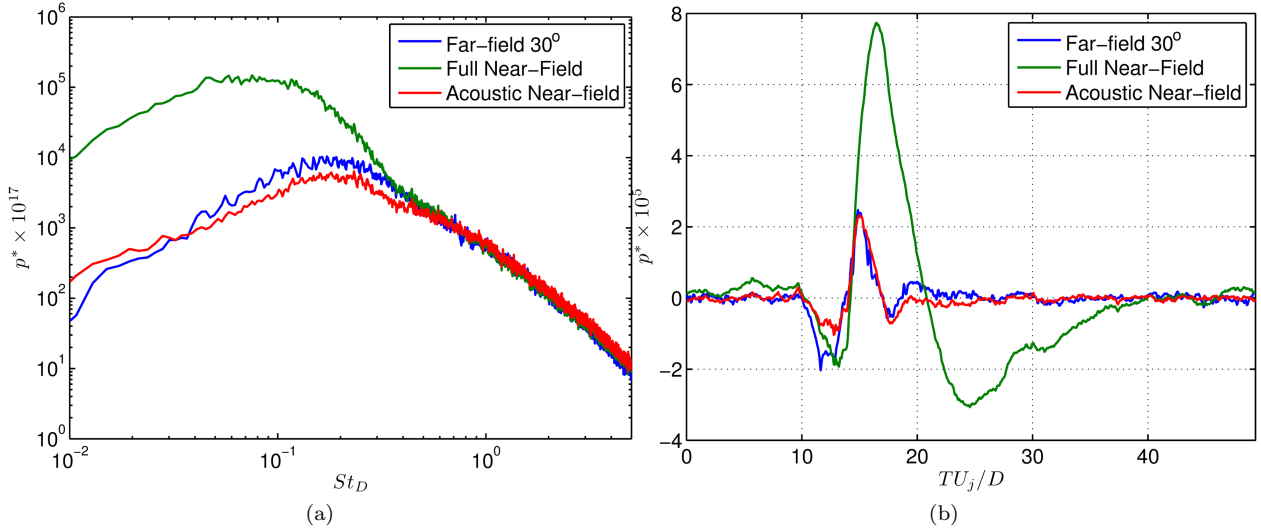


Figure 10: Comparison of full and decomposed near-field signal at $x/D = 8, y/D = 2.2$ propagated to the far-field at 30° , for the natural jet (a) and the jet excited at $St_{DF} = 0.02$ (b).

assumed source region, required to compute τ_{con} and τ_s , is a free parameter that was set by the researchers subsequent to the computation of the two-point correlations in order to best match the observed correlation regions.

Results from the natural jet in the experiment can be found in Fig. 11 for both the full near-field signal and the decomposed acoustic near field. In the full near-field signal, four distinct correlation regions can be observed comprising two physical phenomena. In the most upstream region, the slopes of the correlations match the measured convective velocity of the large scale structures, with the peak correlation occurring just downstream of the end of the potential core ($x/D = 6$). In order to align τ_{con} with the dominant convective correlation region, a source location of $x_s/D = 4$ was found to be necessary. Beyond this location, these correlation regions merge with the second set of correlation regions, which exhibit a slope indicative of acoustically-propagating waves. These correlation regions start from almost negligible values upstream, strongly amplify near and just beyond the end of the potential core, and decay gradually in the downstream region. The behavior of the acoustic correlation regions can, unsurprisingly, be better analyzed using the decomposed acoustic component of the near-field signal. Here, no correlation regions matching the convective velocity of the large-scale structures exist; the convective correlation regions observed in Fig. 11a were associated with the large-scale structures themselves, rather than direct acoustic phenomena. Instead, a single positive correlation region exists over the entire domain, roughly matching with τ_{ac} . A slight discrepancy is observed however in the furthest axial positions, where the positive correlation region instead matches with τ_s , indicating a stationary source region. As before, a source location of $x_s/D = 4$ was found to produce the best match between τ_s and the observed correlation regions. Similar behavior was observed for the excited jet, which for brevity is not included here. In the case of the excited jets, noticeably stronger convective correlations regions were observed, and a periodic pattern of oscillating positive and negative correlation regions, both in the convective and acoustic regions, was observed for the periodically excited jet. Additionally, the source location was found to shift upstream with increasing excitation St_{DF} ; this matches the upstream shift in the saturation point for higher St_{DF} found in Fig. 8. The behavior observed in these plots suggests that the dominant acoustic emissions (at least as identified by linear correlation) are being generated over an extended region of the jet, roughly $x/D \leq 4$, and that this location corresponds to the saturation point of the dominant large-scale structures.

As mentioned previously, analysis of the experimental results can only take the analysis so far, as we are unable to probe inside the mixing layer with both spatial and temporal high-fidelity with current experimental technology. Thus, analysis of the acoustic field embedded in the LES results is paramount. As a preliminary step, the phase-averaged waveforms generated by the excitation were again explored, this time at the furthest spatially resolved axial and radial position simulated (which corresponds to $x/D = 20.0, y/D = 9.0$ - due to computational limitations the acoustic far-field is not simulated), as shown in Fig. 12. Like the

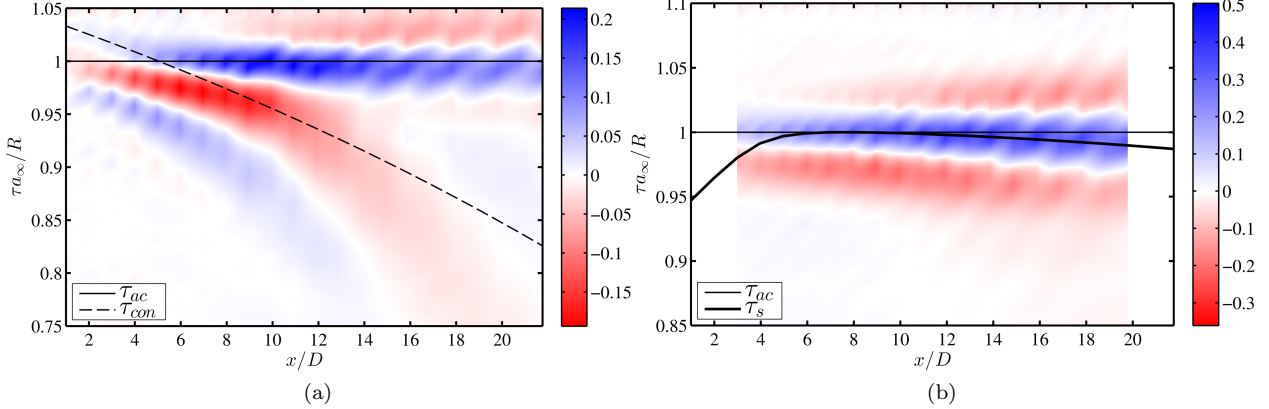


Figure 11: Two-point correlations between the full near-field (a) and acoustic component (b) in the experimental results to the far-field at 30° for the natural jet. The near-field microphones were taken along the first array position, starting at $x/D = 1, y/D = 1.2$. The abscissa has been normalized by the ambient speed of sound and the distance from the near-field microphone to the far-field microphone.

hydrodynamically-dominated waveforms shown in Fig. 6, excitation of the jet at a very low St_{DF} produces a compact, impulsive disturbance in the near acoustic field. And, as before, increasing the excitation frequency results in a periodic wave, one which can be constructed by a linear superposition of the impulse response. For the results of the simulations however, the validity of the linear superposition model break down more quickly than the experiments. While the periodic response at $St_{DF} = 0.15$ can be approximated with the impulse response (Fig. 12b), the periodic response at $St_{DF} = 0.25$ cannot (not shown).

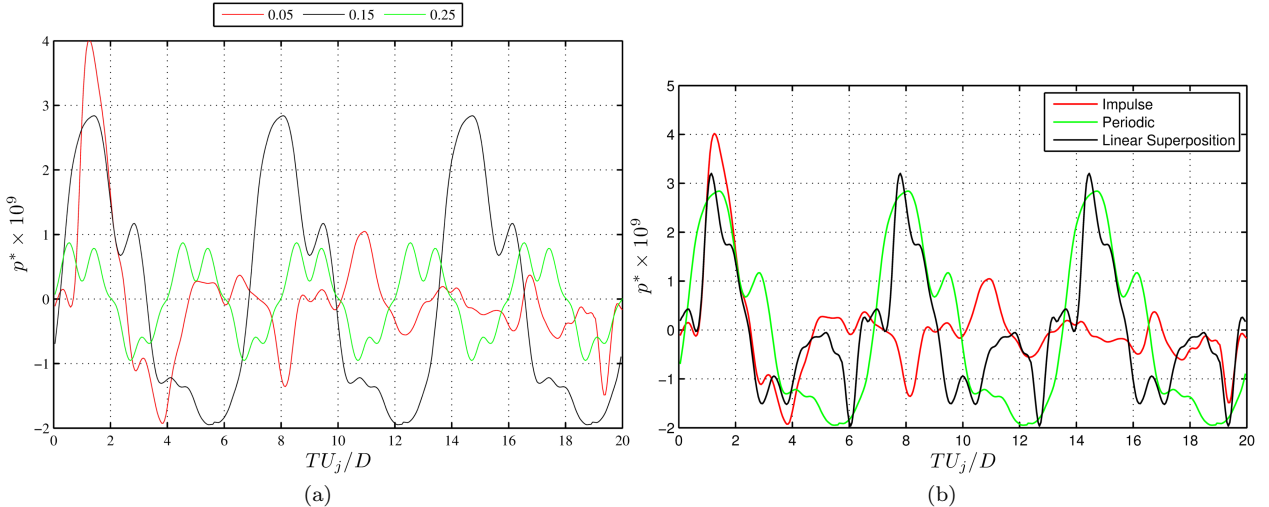


Figure 12: Response to excitation in the simulated jet, phase-averaged waveforms at $x/D = 20.0, y/D = 9.0$ (a) and linear superposition of impulse response as compared against periodic response at $St_{DF} = 0.15$ (b).

Similar to the experimental jet, two-point correlations between the full and decomposed near-field and the furthest axial and radial position were analyzed in order to located the dominant acoustic source region. The full near-field was decomposed using the same methodology as that used for the experimental results. Hence, we are still restricted to decomposing the pressure field along an inclined array just outside the shear layer; as the decomposition occurs only in two dimensions, time and the axial direction, all fluctuations normal to the array appear to have a supersonic phase velocity. If the array were to be located inside the shear layer, hydrodynamic fluctuations in the radial direction are misidentified as acoustic fluctuations. Therefore, the results shown in Fig. 13 used near-field locations which matched the first microphone array location in the experimental results (first microphone starts at $x/D = 1, y/D = 1.2$). Work is currently underway in order to extend the wavelet filtering algorithm to higher spatial dimensions.

Even with the given restrictions, the acoustic source region quickly becomes apparent. As with the experimental results, the simulated results exhibit correlation regions which match quite well with the convective velocity of the large scale structures, especially in the upstream region of the simulated domain. However, in the case of the natural jet correlation regions corresponding to acoustically traveling waves are not readily apparent. It is quite possible that even at $x/D = 20.0, y/D = 9.0$ there is still some hydrodynamic energy which is correlating with the fluctuations near the jet shear layer. A much different picture emerges once the correlations are computed using the acoustic component only; a clear positive correlation region is observed matching with τ_{ac} in the upstream region (corresponding to acoustic waves traveling directly from the noise source to the near-field microphone and on to the 'far-field' microphone). In the downstream region, the positive correlation diverges from this on-axis acoustic propagation and instead follows a curve indicative of off-axis acoustic propagation. For the natural jet, the slope of the divergence indicates an acoustic source region extending over a large portion of the potential core region and ending roughly around $x/D = 10$. This does contrast with the behavior observed in the experimental jet, where the apparent source region in the natural jet is much further upstream and does not differ significantly from the apparent source regions for the excited jets. For $St_{DF} = 0.05$ and 0.25 similar correlation behavior is observed, however here the acoustic source region ends around $x/D = 4$. The reason behind this discrepancy is not currently understood; a possible reasons for this difference could be due to the different frequency content of the natural jet versus the the controlled jets and the close proximity of the near field probe ($x/D = 20, r/D = 9$) to the jet. Future work aims to relate changes in the unexcited flow field to the dynamic interactions observed in the structures generated by forcing in order to shed light on this issue.

V. Conclusions

An unheated, Mach 0.9 jet undergoing excitation with plasma actuators was analyzed using results obtained from experiments and computations to understand the large-scale structure dynamics, and ultimately the noise source mechanism and the resultant acoustic field. Previous experimental work by Sinha *et al.* [17] had found that individual actuation events produce temporally and spatially localized pressure fluctuations in the irrotational near-field - the impulse response of the jet - and the response to periodic excitation could be reconstructed from a linear superposition of this impulse response. In this preliminary work, through the use of phase-averaging and Q-criterion iso-contours, analysis of the numerical results found that this same principle applied inside the jet shear layer, albeit with less accuracy; indicating that the structure interactions are largely (though not entirely) linear in nature. Results also showed that the near and far acoustic field are also governed by this quasi-linear mechanism (though that is not to say that the noise generation process itself is necessarily linear). Although, this linear superpositioning only applied to $St_{DF} < 0.25$ in these regions.

Two-point correlations were then used to compare the irrotational near jet (hydrodynamically dominant) region to the acoustically dominant near and far fields. Results from both the experiments and simulations showed correlation regions matching the convection of the large-scale structures through the jet mixing layer. The full signal of the near field was decomposed into hydrodynamic and acoustic components via a linear filter utilizing a spatio-temporal wavelet transform, and correlations to the near and far acoustic field were recomputed. From these, the dependence of specific regions of the jet to the far field sound was characterized. It was found that the dominant noise source regions (insofar as they correlated best to the near and far acoustic field in a linear sense) comprised an extended region of the jet. However, results diverged between the experiments and simulations as to the exact length of this region. In the experimental jet, the natural as well as the excited cases all indicated that the dominant source region was near or upstream of the end of the potential core (roughly $x/D = 6$), as did the excited cases in the simulated jet. However, the natural jet in the simulated results indicated an apparent source region extended much further downstream, to roughly $x/D = 10$. The cause of this discrepancy is currently under further investigation.

Acknowledgments

Computational resources were provided by the DoD HPCMP (AFRL, NAVO and ERDC) and the Ohio Supercomputer Center. The support of this complementary experimental and computational work by the Air Force Office of Scientific Research (Dr. John Schmisser and Dr. Rengasamy Ponnappan) is greatly appreciated. Several figures were made using Fieldview software with licenses obtained from the Intelligent

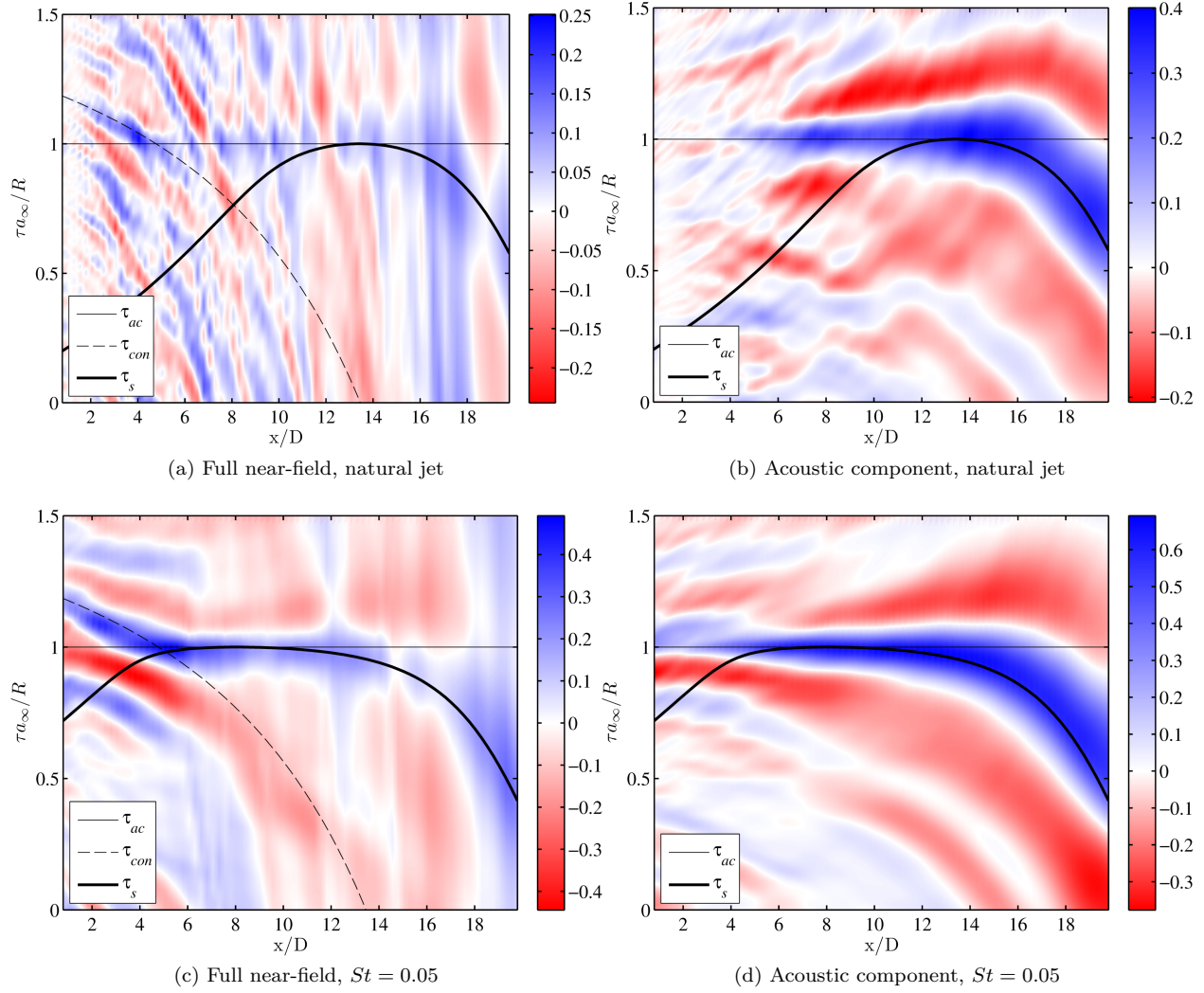


Figure 13: Two-point correlations between the full near-field and acoustic component to the furthest downstream and radial position ($x/D = 20$, $r/D = 9$). Axial and radial positions match the location of the experimental array.

References

- ¹Wei, M. and Freund, J. B., "A noise-controlled free shear flow," *Journal of Fluid Mechanics*, Vol. 546, 2006, pp. pp. 123–152.
- ²Tam, C. K. W., Golebiowski, M., and Seiner, J. M., "On the Two Components of Turbulent Mixing Noise from Supersonic Jets," *AIAA/CEAS 2nd Aeroacoustics Conference*, Vol. AIAA Paper, State College, PA, May 6-8, 1996.
- ³Tam, C. K. W., "Directional acoustic radiation from a supersonic jet generated by shear layer instability," *Journal of Fluid Mechanics*, Vol. 46, No. 4, 1971, pp. pp. 757–768.
- ⁴Tam, C. K. W. and Burton, D. E., "Sound generated by instability waves of supersonic flows. Part 2. Axisymmetric jets," *Journal of Fluid Mechanics*, Vol. 138, 1984, pp. pp. 273–295.
- ⁵Panda, J. and Seasholtz, R. G., "Experimental investigation of density fluctuations in high-speed jets and correlation with generated noise," *Journal of Fluid Mechanics*, Vol. 450, 2002, pp. 97–130.
- ⁶Panda, J., Seasholtz, R. G., and Elam, K. A., "Investigation of noise sources in high-speed jets via correlation measurements," *Journal of Fluid Mechanics*, Vol. 537, 2005, pp. 349–385.
- ⁷Hileman, J., Carabalo, E., Thurow, B., and Samimy, M., "Large-Scale Structure Evolution and Sound Emission in High-Speed Jets: Real-Time Visualization with Simultaneous Acoustic Measurements," *J. Fluid Mech.*, Vol. 544, 2005, pp. 277–307.
- ⁸Sandham, N. D., Morfey, C. L., and Hu, Z. W., "Nonlinear mechanisms of sound generation in a perturbed parallel jet flow," *Journal of Fluid Mechanics*, Vol. 565, 2006, pp. 1–23.
- ⁹Cavalieri, A. V. G., Jordan, P., Gervais, Y., Wei, M., and Freund, J. B., "Intermittent sound generation and its control in a free-shear flow," *Physics of Fluids*, Vol. 22, No. 11, 2010, pp. 115113–.
- ¹⁰Crighton, D. G. and Huerre, P., "Shear-layer pressure fluctuations and superdirective acoustic sources," *Journal of Fluid Mechanics*, Vol. 220, 1990, pp. 355–368.
- ¹¹Samimy, M., Adamovich, I., Webb, B., Kastner, J., Hileman, J., Keshav, S., and Palm, P., "Development and characterization of plasma actuators for high-speed jet control," *Experiments in Fluids*, Vol. 37, No. 4, 2004, pp. 577–588.
- ¹²Utkin, Y., Keshav, S., Kim, J.-H., Kastner, J., Adamovich, I., and Samimy, M., "Use of Localized Arc Filament Plasma Actuators for High Speed Jet Control," *J. Phys. D: Applied Physics*, Vol. 40, Feb 2007, pp. 685–694.
- ¹³Samimy, M., Kim, J.-H., Kastner, J., Adamovich, I., and Utkin, Y., "Active control of high-speed and high-Reynolds-number jets using plasma actuators," *J. Fluid Mech.*, Vol. 578, 2007, pp. 305–330.
- ¹⁴Samimy, M., Kim, J.-H., Kastner, J., Adamovich, I., and Utkin, Y., "Active control of a Mach 0.9 jet for noise mitigation using plasma actuators," *AIAA Journal*, Vol. 45, No. 4, 2007, pp. 890–901.
- ¹⁵Samimy, M., Kearney-Fischer, M., Kim, J.-H., and Sinha, A., "High-Speed and High-Reynolds-Number Jet Control Using Localized Arc Filament Plasma Actuators," *Journal of Propulsion and Power*, Vol. 28, No. 2, 2012, pp. 269–280.
- ¹⁶Kearney-Fischer, M., Kim, J.-H., and Samimy, M., "A Study of Mach Wave Radiation Using Active Control," *Journal of Fluid Mechanics*, Vol. 681, 2011, pp. 261–292.
- ¹⁷Sinha, A., Alkandry, H., Kearney-Fischer, M., Samimy, M., and Colonius, T., "The Impulse Response of a High-Speed Jet Forced with Localized Arc Filament Plasma Actuators," *Physics of Fluids*, 2013.
- ¹⁸Crawley, M., Sinha, A., and Samimy, M., "Near-field and Acoustic Far-field Response of a High-Speed Jet Forced with Plasma Actuators," *AIAA Journal*, Accept, awaiting publication.
- ¹⁹Gaitonde, D. and Samimy, M., "Coherent structures in plasma-actuator controlled supersonic jets: Axisymmetric and mixed azimuthal modes," *Phys. Fluids*, Vol. 23, No. 9, 2011.
- ²⁰Speth, R. and Gaitonde, D., "Near Field Pressure and Associated Coherent Structures of Excited Jets," *4th Joint US-European Fluids Engineering Summer Meeting*, , No. FEDSM2014-21186, 2014.
- ²¹Speth, R. and Gaitonde, D., "Correlation of Near Field Pressure with Coherent Structures in an Excited Mach 1.3 Jet," *ASME 2013 Fluids Engineering Division Summer Meeting*, No. FEDSM2013-16495, 2013.
- ²²Hahn, C., *Design and Validation of the New Jet Facility and Anechoic Chamber*, Ph.D. thesis, The Ohio State University, Columbus, OH, 2011.
- ²³Kearney-Fischer, M., Kim, J.-H., and Samimy, M., "Control of a High Reynolds Number Mach 0.9 Heated Jet Using Plasma Actuators," *Physics of Fluids*, Vol. 21, No. 9, 2009.
- ²⁴Utkin, Y., Keshav, S., Kim, J.-H., Kastner, J., Adamovich, I., and Samimy, M., "Characterization of Localized Arc Filament Plasma Actuators Used for High-speed Flow Control," *AIAA Paper 2007-0787*, 2007.
- ²⁵Hahn, C., Kearney-Fischer, M., and Samimy, M., "On factors influencing arc filament plasma actuator performance in control of high speed jets," *Experiments in Fluids*, Vol. 51, No. 6, 2011, pp. 1591–1603.
- ²⁶Speth, R. and Gaitonde, D., "Parametric Study of a Mach 1.3 Cold Jet Excited by the Flapping Mode Using Plasma Actuators," *Computers & Fluids*, 2013.
- ²⁷Vinokur, M., "Conservation Equations of Gasdynamics in Curvilinear Coordinate Systems," *J. Comp. Phys.*, Vol. 14, 1974, pp. 105–125.
- ²⁸Steger, J., "Implicit Finite-Difference Simulation of Flow about Arbitrary Two-Dimensional Geometries," *AIAA Journal*, Vol. 16, No. 7, July 1978, pp. 679–686.
- ²⁹Speth, R. and Gaitonde, D., "The Effect of Laminar Nozzle Exit Boundary Layer Thickness on a Mach 1.3 Jet With and Without Control," *42nd AIAA Fluid Dynamics Conference and Exhibit*, 2012.
- ³⁰Roe, P., "Approximate Riemann Solvers, Parameter Vectors and Difference Schemes," *Journal of Computational Physics*, Vol. 43, 1981, pp. 357–372.
- ³¹van Leer, B., "Towards the Ultimate Conservation Difference Scheme V, A Second-Order Sequel to Godunov's Method," *Journal of Computational Physics*, Vol. 32, 1979, pp. 101–136.

- ³²Pulliam, T. and Chaussee, D., "A Diagonal Form of an Implicit Approximate-Factorization Algorithm," *J. Comp. Phys.*, Vol. 39, No. 2, 1981, pp. 347–363.
- ³³Beam, R. and Warming, R., "An Implicit Factored Scheme for the Compressible Navier-Stokes Equations," *AIAA Journal*, Vol. 16, No. 4, 1978, pp. 393–402.
- ³⁴Bellan, J., "Supercritical (and Subcritical) Fluid Behavior and Modeling: Drops, Streams, Shear and Mixing Layers, Jets and Sprays," *Prog. Energy Combust. Sci.*, Vol. 26, 2000, pp. 329–366.
- ³⁵Speth, R. and Gaitonde, D., "Parametric Study of a Supersonic Jet Subjected to Plasma-based Flapping Mode Excitation," *AIAA Paper 2012-0901*, 2012.
- ³⁶Gaitonde, D., "Analysis of plasma-based flow control mechanisms through large-eddy simulations," *Computers and Fluids*, Vol. 85, 2013, pp. 19–26.
- ³⁷Cohen, J. and Wygnanski, I., "The evolution of instabilities in the axisymmetric jet. Part 2. The flow resulting from the interaction between two waves," *J. Fluid Mech.*, Vol. 176, 1987, pp. 221–235.
- ³⁸Hussain, A. and Reynolds, W., "The mechanisms of an organized wave in turbulent shear flow," *J. Fluid Mech.*, Vol. 41, No. 2, 1970, pp. 241–258.
- ³⁹Arndt, R. E. A., Long, D. F., and Glauser, M. N., "The proper orthogonal decomposition of pressure fluctuations surrounding a turbulent jet," *Journal of Fluid Mechanics*, Vol. 340, 1997, pp. 1–33.
- ⁴⁰Gaitonde, D., "Analysis of the Near Field in a Plasma-Actuator-Controlled Supersonic Jet," *J. Prop. Power*, Vol. 28, No. 2, March-April, 2012 2012, pp. 281–292.
- ⁴¹Suzuki, T. and Colonius, T., "Instability waves in a subsonic round jet detected using a near-field phased microphone array," *Journal of Fluid Mechanics*, Vol. 565, 2006, pp. 197–226.
- ⁴²Ukeiley, L. S. and Ponton, M. K., "On the near field pressure of a transonic jet," *International Journal of Aeroacoustics*, Vol. 3, No. 1, 2004, pp. 43–66.
- ⁴³Coiffet, F., Jordan, P., Delville, J., Gervais, Y., and Ricaud, F., "Coherent structures in subsonic jets: a quasi-irrotational source mechanism?" *International Journal of Aeroacoustics*, Vol. 5, No. 1, 2006, pp. 67 – 89.
- ⁴⁴Tinney, C. E. and Jordan, P., "The near pressure field of co-axial subsonic jets," *Journal of Fluid Mechanics*, Vol. 611, 2008, pp. 175–204.
- ⁴⁵Crawley, M. and Samimy, M., "Decomposition of the Near-field Pressure in a Forced Subsonic Jet," *20th AIAA/CEAS Aeroacoustics Conference*, June 2014.
- ⁴⁶Bogey, C. and Bailly, C., "An analysis of the correlations between the turbulent flow and the sound pressure fields of subsonic jets," *J. Fluid Mech.*, Vol. 583, 2007, pp. 71–97.